Modeling and simulation of flexible needles

Orcun Goksel*, Ehsan Dehghan, Septimiu E. Salcudean

The Department of Electrical and Computer Engineering, University of British Columbia, 2332 Main Mall, Vancouver, BC, Canada V6T1Z4

A B S T R A C T

Needle insertion is performed in many clinical and therapeutic procedures. Tissue displacement and needle bending which result from needle–tissue interaction make accurate targeting difficult. For performing physicians to gain essential needle targeting skills, needle insertion simulators can be used for training. An accurate needle bending model is essential for such simulators. These bending models are also needed for needle path planning.

In this paper, three different models are presented to simulate the deformations of a needle. The first two models use the finite element method and take the geometric nonlinearity into account. The third model is a series of rigid bars connected by angular springs. The models were compared to recorded deformations during experiments of applying lateral tip forces on a brachytherapy needle. The model parameters were identified and the simulation results were compared to the experimental data. The results show that the angular spring model, which is computationally the most efficient model, is also the most accurate in modeling the bending of the brachytherapy needle.

© 2009 IPEM. Published by Elsevier Ltd. All rights reserved.

1. Introduction

Percutaneous insertion of long and flexible needles into soft tissue is involved in many clinical and therapeutic procedures such as biopsy and prostate brachytherapy. As a result of needle–tissue interaction, the needle base movements and, for needles with a beveled tip, the asymmetric cutting force on the tip, the tissue deforms and the needle bends (see Fig. 1). The targeting procedure is complicated by the bending of the needle shaft, target displacement due to tissue deformation, and insufficient visual feedback from medical imaging modalities. Accurate needle insertion requires significant skill and training of the performing physician. Modeling, simulation, and path planning of needle insertion are emerging fields of research aimed at providing the physicians with training devices and accurate pre-surgery plans.

Needle insertion simulators usually include a soft tissue model, a flexible needle model and a needle–tissue interaction model. The simulation of needle bending and tissue deformation together in one combined model is generally not feasible for two reasons: (i) a fast solution for a large tissue mesh requires exploiting simplifications in deformation equations, which are not suitable for estimating the needle behavior and (ii) the interaction surface of the needle and tissue changes during insertion, which many techniques like the finite element method (FEM) cannot inherently accommodate. Therefore, generally two separate models for the tissue and the needle are employed [1–4] with a third needle–tissue contact model governing their interaction.

Deformable tissue models have been studied extensively in simulating tissue deformation during surgery and needle insertion [1–5]. Models based on the FEM are the most common techniques employed for tissue deformation simulation during needle insertion [1,2,4,6]. Mass-spring models [7] have also been used for this purpose. The interaction of needles with such deformable tissue models has been studied widely [2,8,9,5].

The aim of this paper, the preliminary results of which were presented in [10], is to compare different models for simulating the bending of flexible needles. In general, medical needles can be categorized into three major groups: rigid needles, highly flexible needles, and (moderately) flexible needles. Rigid needles keep a straight posture regardless of the forces applied on them during insertion. Due to their simplicity, rigid needle models have been used when the needle physical properties and the insertion procedure lead to negligible bending [2,1,6]. On the opposite end of the flexibility range are the *highly* flexible needles. These needles are assumed to bend in the direction of their tip bevel with a constant curvature, without applying considerable force to the tissue in the lateral direction. These needles were modeled as a non-holonomic system [3] and were used for needle insertion simulations and planning in [11–13].

Some needles, such as brachytherapy needles, cannot be categorized as either rigid or highly flexible. They are not rigid, since their deflection during procedures is significant. They are not

* Corresponding author.
 E-mail addresses: orcung@ece.ubc.ca (O. Goksel), ehsand@ece.ubc.ca (E. Dehghan), tims@ece.ubc.ca (S.E. Salcudean).
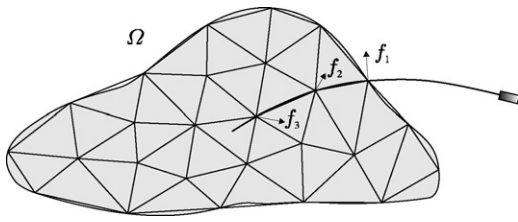
Fig. 1. The forces on the needle shaft caused by tissue deformation and needle base manipulation.

highly flexible either, since a considerable lateral force is necessary to bend them. Several groups have modeled this type of needles. DiMaio and Salcudean simulated the needle as an elastic material using FEM with geometric nonlinearity and 3-node triangular elements and validated this method in phantom studies [14]. This method was extended to 3D using 4-node tetrahedral elements by Goksel et al. [4]. Glozman and Shoham used linear 2D beam elements to simulate the needle bending for needle steering [7]. Linear beam theory was also used to introduce a needle steering model with online parameter estimator [15], to estimate the needle tip deflection during insertion due to tip bevel [16], and to identify the shaft force profile due to the bevel [17]. Models based on linear beam theory are relatively simple and fast. However, they are not rotationally invariant and cannot preserve the needle length during large deformations/deflections.

Many needles, such as brachytherapy needles, consist of a stylet sliding inside a hollow cannula. Physical modeling of this combination without any simplifications is indeed very complicated as it requires separate models for the stylet and the cannula and an interaction model to simulate their interface. In this paper, flexible needles are approximated as solid bars and, accordingly, models applicable to solid bars are examined to simulate their flexion.

Three different models were used to simulate needle bending. The first two models are based on the FEM and were chosen due to their frequent use in the literature, while the third model is an angular springs model. The first model uses 4-node tetrahedral elements, where nonlinear geometry is accommodated to simulate large deformations. The second model also accommodates nonlinear geometry and uses Euler–Bernoulli nonlinear beam elements. In this work, nonlinear beam elements were preferred over more common linear ones in the literature due to their superiority in modeling large deformations. The third model is novel and utilizes angular springs for the quasi-static simulation of needle bending. In the literature, angular springs have been used to model cantilever-like structures [18] such as beams in mechanical engineering [19] and hair deformation in computer graphics [20]. They have been also incorporated in 3D mass-spring models to simulate large volume deformations [21]. In this paper, this type of a spring model is implemented using finite-differences for medical needles, for which its performance is compared with two other common types of physically based models using FEM.

The Young's modulus is the parameter that describes needle bending in the first two models. Similarly, the third model is identified by its spring constant. In contrast to [10], in this paper all models are devised for needle bending in 3D. The parameter of each model is identified for a brachytherapy needle through experiments, where several lateral forces were applied to the needle tip and the shaft deflection was recorded. The parameters defining each model were identified and the models were studied for their accuracy in simulating the actual needle deflection observed during experiments.

In this paper, the needle bending models are derived in 3D, since their formulations are applicable in 3D settings as well as in 2D. Note that, for the single force applied at the needle tip during the experiments, the needle deformation is entirely planar. Therefore, the parameter identification and the model validations were performed in 2D. Nevertheless, the same identified parameters also describe a needle in 3D, since the shafts of most medical needles are built with axial symmetry resulting in symmetric deflection for the same force rotated around their long axis.

The following section derives the models in 3D. Next, the experimental method to validate the models is described in Section 3. The results and a discussion follow in Sections 4 and 5, respectively. Finally, conclusions are presented in the last section.

2. Methods

2.1. Finite element method using tetrahedral elements

The finite element method is a powerful tool for approximating a solution to the continuum mechanics equations. In this method, an entire body Ω is divided into several discrete elements Ω_e. Then, the constitutive equations are approximated over each element and combined to give an approximation to the global solution. Various types of elements can be chosen depending on the nature of the problem. 4-Node tetrahedral (TET4) or 3-node triangular (TRI3) elements are the simplest elements to use in 3D or 2D deformation analysis, respectively.

Considering a deformable body, the 3D coordinates of a point in the undeformed configuration can be written as $[x_1\, x_2\, x_3]$ in the reference frame. The coordinates of that point in the deformed configuration can then be expressed using the displacements $[u_1\, u_2\, u_3]$ added onto the undeformed coordinates. Using this definition, the Green strain and the second Piola–Kirchhoff stress tensors are given as follows:

$$\epsilon_{ij} = \frac{1}{2}\left(\frac{\partial u_i}{\partial x_j} + \frac{\partial u_j}{\partial x_i} + \sum_{k=1}^{3}\frac{\partial u_k}{\partial x_i}\frac{\partial u_k}{\partial x_j}\right),\tag{1}$$

$$\sigma_{ij} = \sum_{k=1}^{3}\sum_{l=1}^{3}\mathbf{C}_{ijkl}\,\epsilon_{kl},\tag{2}$$

where $i, j \in \{1, 2, 3\}$ and $\mathbf{C}_{ijkl}$ is the material moduli tensor for linear elastic materials which is a function of Young's modulus and Poisson's ratio.

When the deformation is small, the second order terms in (1) can be neglected leading to a linear relation between strain and displacement. This linear relation leads to a set of linear algebraic equations with a constant coefficient matrix. Such a system can be solved rapidly using off-line computation and condensation [2,22]. However, the assumption of small deformation is not valid for needle bending, where the deformation is large with respect to the needle diameter [14]. Thus, nonlinear geometry as in (1) must be included in the model. This leads to a nonlinear relation between the nodal forces and displacements:

$$\underline{f} = \hat{\mathbf{K}}(\underline{u})\,\underline{u}\tag{3}$$

where $\underline{u}$ and $\underline{f}$ are the vectors of nodal displacements and forces, respectively, and $\hat{\mathbf{K}}$ is the stiffness matrix, the elements of which can be represented as functions of nodal displacements $\underline{u}$. This nonlinear equation can accommodate the axial displacements during lateral deformation and, therefore, preserves the needle length. However, the use of condensation is not possible in the nonlinear case and this leads to a time-consuming solution.

The Newton–Raphson method is an effective iterative technique for solving the nonlinear algebraic equations in (3)[23]. In this method, a tangent stiffness matrix $\mathbf{K}_T$ is computed at each iteration and used to find a descent direction for the solution using the
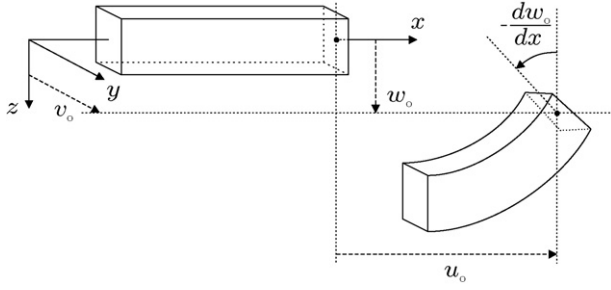
Fig. 2. Euler–Bernoulli beam element under deformation.

iteration scheme below:

$$\mathbf{K}_T \Delta \underline{u}^t = \underline{f} - \hat{\mathbf{K}}(\underline{u}^t)\underline{u}^t \tag{4}$$

$$\underline{u}^{t+1} = \underline{u}^t + \Delta \underline{u}^t \tag{5}$$

to update the nodal displacements at each iteration t.

In our simulations, the Newton–Raphson method converged to a solution for (3) in a few iterations. Unfortunately, computing the tangent stiffness matrix and solving (4) at each iteration are both computationally intensive operations.

2.2. Finite element method using nonlinear beam elements

Beam elements were designed and introduced in the FEM literature in order to model the deformation of bars, rods, and other beam-like structures [24]. These elements are expected to be better suited for needle deformations than triangular/tetrahedral elements. Thus, a beam element model was also implemented to compare its performance in modeling needles. Euler–Bernoulli beam element is a common element formulation to model thin bars and therefore is used as a needle model in this paper.

Euler–Bernoulli beam theory suggests that each plane perpendicular to the beam axis prior to any deformation remains as a plane that is still perpendicular to the beam axis after the deformation. Under this condition the displacements of each material point can be written as a function of the displacement along the neutral axis of the beam as follows:

$$u(x, y, z) = u_0(x) - y\frac{\partial v_0(x)}{\partial x} - z\frac{\partial w_0(x)}{\partial x}, \tag{6}$$

$$v(x, y, z) = v_0(x) - z\alpha_0(x), \tag{7}$$

$$w(x, y, z) = w_0(x) + y\alpha_0(x), \tag{8}$$

where u_0, v_0, and w_0 are the neutral axis displacements along the x, y, and z axes, respectively, and α_0 is the twist around the beam axis. It is assumed that the beam axis is lying along the x axis as shown in Fig. 2. Please note that, in order to conform to the beam element literature, the node positions $[x_1 \, x_2 \, x_3]$ and the node displacements $[u_1 \, u_2 \, u_3]$ in the previous subsection are referred here as $[x \, y \, z]$ and $[u \, v \, w]$, respectively.

Assuming that the beam twist is small while the lateral deformations are moderately large, strains in the beam element can be approximated as [25]:

$$\epsilon_{xx} \approx \frac{du_0}{dx} - y\frac{d^2v_0}{dx^2} - z\frac{d^2w_0}{dx^2} + \frac{1}{2}\left(\left(\frac{dv_0}{dx}\right)^2 + \left(\frac{dw_0}{dx}\right)^2\right), \tag{9}$$

$$\epsilon_{xy} \approx -\frac{1}{2}z\frac{d\alpha_0}{dx}, \tag{10}$$

$$\epsilon_{xz} \approx \frac{1}{2}y\frac{d\alpha_0}{dx}. \tag{11}$$

In the beam element, the displacements of the material nodes on the beam axis are interpolated from the nodal variables of the
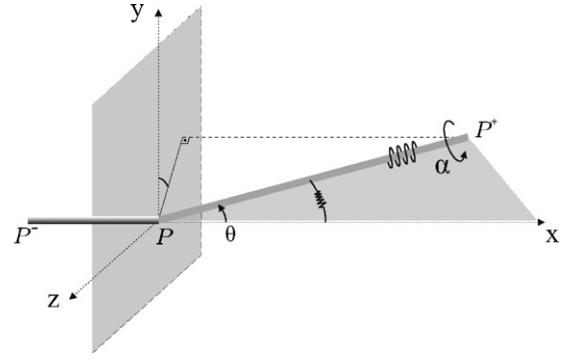

Fig. 3. Angles of bending and twisting between two needle segments.

two end-points (nodes) of the beam. The nodal variables at node p are the axial displacement u_p, the twist α_p, the transverse displacements v_p and w_p (along the y and z axes, respectively), and their derivatives $\phi_p = -dv/dx$ and $\psi_p = -dw/dx$. Euler–Bernoulli beam theory employs cubic interpolation functions for lateral displacements, and linear interpolation functions for axial displacements and twist angle. Therefore, within each element between nodes p and $p+1$, the variables are interpolated as follows:

$$u_0(x) = N_1(x)u_p + N_2(x)u_{p+1} \tag{12}$$

$$\alpha_0(x) = N_1(x)\alpha_p + N_2(x)\alpha_{p+1} \tag{13}$$

$$v_0(x) = M_1(x)v_p + M_2(x)\phi_p + M_3(x)v_{p+1} + M_4(x)\phi_{p+1} \tag{14}$$

$$w_0(x) = M_1(x)w_p + M_2(x)\psi_p + M_3(x)w_{p+1} + M_4(x)\psi_{p+1} \tag{15}$$

where $N_i(x)$ and $M_i(x)$ denote the linear and cubic interpolation functions, respectively.

An element equilibrium equation relating loads on the nodes to the nodal variables is written as:

$$\mathbf{K}(\underline{u})\underline{u} = \underline{f}, \tag{16}$$

where $\underline{u}$ is the vector of nodal variables described above and $\underline{f}$ is the vector of corresponding nodal forces and torques. Please see Appendix A for detailed information on the calculation of the stiffness matrix and its integration. To solve (16), Picard's method [24] is used in this paper. This method employs the following iterative steps:

$$\mathbf{K}(\underline{u}^t)\underline{u}^{t+1} = \underline{f} \tag{17}$$

where t is the iteration number.

2.3. Angular springs model

In this section, the needle is modeled as a discrete structure composed of n connected rigid rods. A joint P between two consecutive segments of such a model is shown in Fig. 3, where the segment PP^+ is bent and twisted relative to the segment before it, P^-P, under external loads. The magnitude of bending and twisting can be described by two angles: the bending (zenith) angle θ from the x axis to the segment PP^+, and the twisting angle α about the segment PP^+ due to torsion around its axis.

Naturally, a deformed (bent and twisted) needle structure applies internal reaction ("straightening") torques/forces to *un-bend* and *un-twist* itself. These are modeled as torques applied to link PP^+ at joint P to restore its rest configuration. The effect of these torques can be visualized as two rotational springs – one unbending and the other un-twisting the segment – shown in Fig. 3. It is evident that the magnitudes of such restoring torques are functions of the deviations (angles θ and α) from the rest configuration.
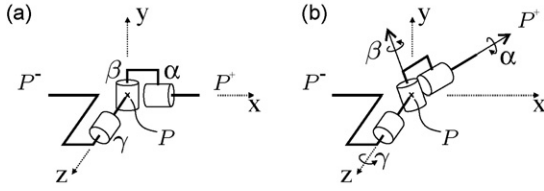
(a)

(b)

Fig. 4. Three joints of our spherical wrist model in (a) initial and (b) bent configurations.

Let us define the magnitudes of these reaction torques, τ_b for bending and τ_t for twisting, as functions of the angles as follows:

$$\tau_b = h_b(\theta), \tag{18}$$

$$\tau_t = h_t(\alpha). \tag{19}$$

Although the actual characteristics of h_b and h_t may be complex and possibly nonlinear, for the elastic range of deformations, a linear relationship is expected. Indeed, when an infinitesimal section of a cantilever shaft is analyzed for its bending (in Appendix B) and its twisting (in Appendix C), linear angle-torque dependencies are observed for both of them. These insights motivate us to devise our model composed of linearly acting springs as follows:

$$\tau_b = k_b\theta, \tag{20}$$

$$\tau_t = k_t\alpha. \tag{21}$$

Then, the energy stored in these springs can be written as:

$$V(\theta, \alpha) = \frac{1}{2}k_b\theta^2 + \frac{1}{2}k_t\alpha^2. \tag{22}$$

As a model of the connections between each pair of segments, a spherical wrist – the rest configuration of which is shown in Fig. 4(a) – is chosen in this paper. These three wrist joints, seen in a bent/twisted configuration in Fig. 4(b), define the orientation of the segment to its right with respect to the segment to its left. Note that, whereas the third joint α defines the twisting angle independently, the bending angle θ is a combination of the joint angles γ and β. It can be geometrically shown that:

$$\cos\theta = \cos\gamma \cos\beta. \tag{23}$$

In order to derive compliance models for the joints γ and β, let us rewrite the energy as a function of these joint variables, e.g. $V(\gamma, \beta, \alpha)$. For sufficiently small angles, $\theta \approx \sin\theta$. This greatly simplifies the following derivation and the solution of final system of equations. Thus, replacing $\theta^2 = \sin^2\theta$ and (23) in (22):

$$V(\theta, \alpha) = \frac{1}{2}k_b(1 - \cos^2\theta) + \frac{1}{2}k_t\alpha^2, \tag{24}$$

$$V(\gamma, \beta, \alpha) = \frac{1}{2}k_b(1 - \cos^2\gamma \cos^2\beta) + \frac{1}{2}k_t\alpha^2. \tag{25}$$

Considering the invariance of the Langrangian at equilibrium, the partial derivatives of joint angles are equal to joint torques,

which are the gradients of the potential with respect to the joint angle coordinates, as follows:

$$\tau_\gamma = \frac{\partial V}{\partial \gamma} = k_b \sin\gamma \cos\gamma \cos^2\beta, \tag{26}$$

$$\tau_\beta = \frac{\partial V}{\partial \beta} = k_b \sin\beta \cos\beta \cos^2\gamma, \tag{27}$$

$$\tau_\alpha = \frac{\partial V}{\partial \alpha} = k_t\alpha. \tag{28}$$

The small angle approximation above also applies to γ and β, i.e. $\sin\gamma \approx \gamma$, $\sin\beta \approx \beta$, $\cos\gamma \approx 1$, and $\cos\beta \approx 1$, thus yielding:

$$\tau_\gamma \approx k_b\gamma, \tag{29}$$

$$\tau_\beta \approx k_b\beta. \tag{30}$$

Consider a 3D bent needle posture in equilibrium with force loads $\underline{f}_i$ applied at its joints as in Fig. 5. Using our spherical wrist model, a Jacobian matrix $\boldsymbol{J}$ can be written for this $3n$-joint robotic arm [26], where the joint torques $\underline{\tau} = [\underline{\tau}'_1 \ldots \underline{\tau}'_n]'$ relate to forces $\underline{f}$ as follows:

$$\underline{\tau} = \boldsymbol{J}'\underline{f}. \tag{31}$$

From (28)–(30), the $3n$ vector of joint torques $\underline{\tau}$ can be written as a combination of $3n$ joint angles $\underline{\Phi} = \begin{bmatrix} \gamma_1 \beta_1 \alpha_1 \ldots \gamma_n \beta_n \alpha_n \end{bmatrix}'$ and the corresponding joint stiffnesses as follows:

$$\underline{\tau} = \boldsymbol{K_s}\underline{\Phi} \tag{32}$$

where $\boldsymbol{K_s}$ is a diagonal matrix formed by joint stiffnesses $\{k_{b,1} \, k_{b,1} \, k_{t,1} \ldots k_{b,n} \, k_{b,n} \, k_{t,n}\}$.

Note that since the Jacobian $\boldsymbol{J}$ is configuration dependent, (31) is indeed a nonlinear system of equations as follows:

$$\boldsymbol{K_s}\underline{\Phi} = \boldsymbol{J}'(\underline{\Phi})\underline{f}. \tag{33}$$

In this paper, this nonlinear system is solved iteratively using Picard's method:

$$\underline{\Phi}^{t+1} = \boldsymbol{K_s}^{-1}\boldsymbol{J}'(\underline{\Phi}^t)\underline{f} \tag{34}$$

which consists of two phases: (i) given the needle configuration, the Jacobian is composed, and (ii) the torques found by $\boldsymbol{J}'\underline{f}$ are divided by corresponding joint stiffnesses to find the joint angles and hence the needle posture at the next iteration.

2.4. A common convergence criterion for all models

In order to have a fair comparison between the three needle models, a common convergence criterion was devised to be used in the simulations as follows:

$$Error = \frac{\|\underline{u}^t - \underline{u}^{t-1}\|}{\|\underline{u}^t\|} < \lambda \tag{35}$$

where $\underline{u}^t$ is the vector of nodal displacements at the iteration t and λ is the tolerance. In this paper, a tolerance of 10^{-4} is used.

When the convergence criterion in (35) is met, the residual of error for all the models were checked to ensure convergence. For the
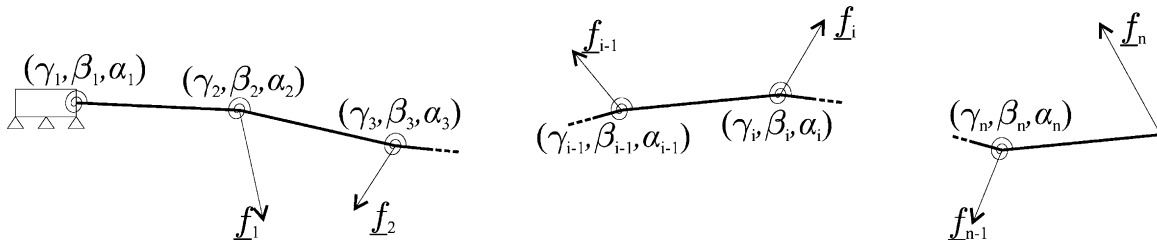

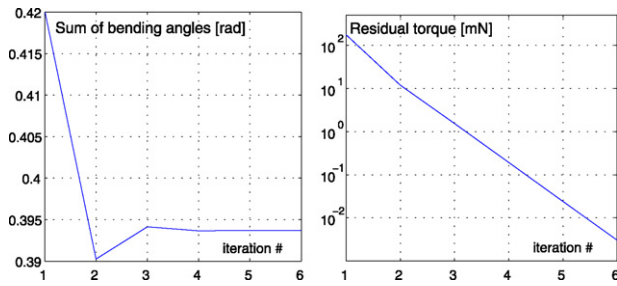**Fig. 5.** The entire needle in equilibrium state constrained at the base and under nodal forces at its joints.

Fig. 6. For a sample bending simulation, (a) shows the sum of joint angles γ, which is the deflection of the needle tip, and (b) shows the residual torque at each iteration.

proposed angular springs model in (33), that is the torque residual $\left| J'(\underline{\Phi}^t)f - K_s\underline{\Phi}^t \right|$. For all the simulations in this paper, the terminal residuals of the three models were sufficiently small indicating model convergence to equilibrium.

Fig. 6 shows the convergence during a sample planar deflection with a tip force applied in $-y$ direction. The sum of angles γ is plotted in Fig. 6(a). Note that for this planar bending, this sum is equal to the deflection angle of the needle tip with respect to the needle base frame lying along x axis. The torque residual during this simulation is also plotted in Fig. 6(b).

3. Experiment

In order to show the feasibility of the models and compare their accuracy, the following experiments were conducted using an 18 gauge 20 cm Bard ® BrachyStar ® needle (C.R. Bard, Inc., Covington, GA), that is used in prostate brachytherapy seed-implant procedures. In these experiments, the needle was bent under several known forces and its bent shaft form is recorded for evaluating our model simulations.

During the experiments, the needle was clamped at its base while its shaft lay horizontal to the ground. Due to the clamping mechanism, the effective bending shaft-length of the needle was reduced to 18.7 cm. Subsequently, several vertical forces were applied to its tip using combinations of scaling weights. The weights were placed on a stage hanging on a tiny hook bent at the tip in order to achieve a perpendicular force to the needle base at all times. The stage setup for hanging weighs 1.3 g and the weights applied were 5, 10, 15, 20, 25, 30, and 40 g.

For each force applied, the needle was imaged as in Fig. 7 over a white background using a digital camera, the shutter of which was controlled via computer. Ordinary brachytherapy needles are marked with black stripes at every 1 cm. These markers were located on each image to determine the bent configuration of the needle. Needle-tip lateral deflections from the nominal axis, measured using this procedure, are shown in Table 1.

To minimize the effect of lens warping on the data, the needle was centered close to the image center and a far camera focal distance was used. By imaging straight lines, this effect was found to be negligible in the given setup. In a calibration step using a ruler,
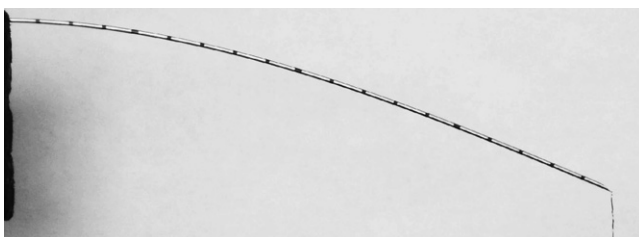
Table 1
Tip deflection for various lateral tip forces.

Force [mN]	63	113	163	213	263	313	413
Deflection [mm]	8.3	14.5	20.9	27.0	33.0	39.0	50.2

the image resolution on the needle plane was measured to be better than 9 pixels/mm.

The observations of shaft bending in these experiments were next used to (i) identify the model parameters for the given brachytherapy needle, and (ii) evaluate the accuracy of each model by comparing the simulated bent needles to the experimental data.

4. Results

In the experiments, the needle deformations were all planar. Therefore, the model equations were reduced to their 2D equivalents. The equations for a 2D nonlinear beam element are obtained by simply removing the rows and columns of the stiffness matrix in (16) that correspond to v, ϕ and α in the vector of nodal variables (reducing $\mathbf{K}$ to its parts $\mathbf{K}^{11}$, $\mathbf{K}^{13}$, $\mathbf{K}^{31}$, and $\mathbf{K}^{33}$ in Appendix A). The angular spring model can be used in 2D simply by neglecting the torsion. The FEM with tetrahedral elements reduces to triangular elements in 2D. A 2D plane-stress analysis was then performed by also taking the out-of-plane thickness of the elements into account. The Poisson's ratio was taken to be 0.3, which is the Poisson's ratio of steel. Therefore, the model parameters to be identified are the Young's modulus E in the two FEM-based models and the bending spring constant k_b in the angular spring model. Equal-length segments were chosen so that the needle bending is described by a single parameter in each model.

4.1. Parameter identification

For parameter identification, two independent goals were specified: (i) a best fit to the experimental tip position, and (ii) a best fit of the entire needle shaft. Accordingly, two cost functions relating an actual bending to a simulated one were defined as seen in Fig. 8: (i) a lateral tip position error, that is, the vertical difference between the simulated and the measured tip position, and (ii) the area lying between the simulated and the observed needle shafts. These goals, namely the *tip fit* and the *area fit*, were formulated as two separate optimization problems. Subsequently, the model parameters were found for each of them, independently, using the Nelder-Mead simplex search method [27].

In the first phase the model parameters were identified for different numbers of elements using each pair of force–displacement data. The effect of the number of elements on the identified parameters and the accuracy of the simulation were studied using models with 10 and 20 segments. In the triangular FEM model, meshes with 11×2 and 21×2 nodes were employed corresponding to 10 and 20 segments, respectively. The 11×2 triangular mesh employed is seen in Fig. 9, where the shaft thickness was set to that of a brachytherapy needle.

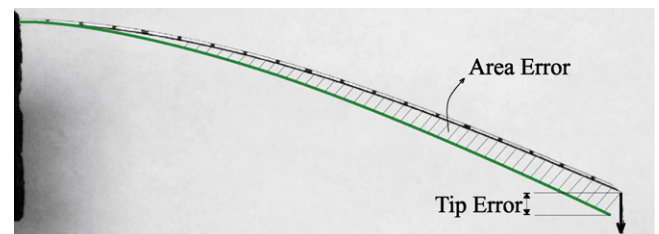**Fig. 7.** Needle shaft clamped at its base a vertical force is applied at its tip

Fig. 8. The definitions of the tip error and the area error between the simulated model and the observed needle postures.
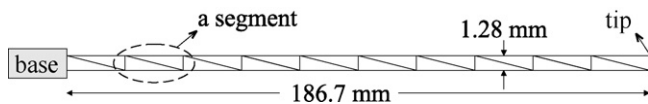
Fig. 9. Needle discretized by triangular elements on a 11 × 2 mesh.

Fig. 10 shows the range of the identified Young's moduli and the identified angular spring constants over the range of applied forces for different numbers of segments. In this figure, the identified parameters for both optimization goals are presented as box-plots displaying the distribution of parameters for varying tip loads.

Fig. 10(a) presents the identified bending spring constants for 10, 20, and 50 segments. Similarly, Fig. 10(b) presents the identified Young's moduli for 10 and 20 triangular elements. As seen in the plots, Young's modulus for triangular elements and spring constants for angular springs are highly dependent on the number of segments. This is due to the nature of these models where adding segments increases the shaft flexibility since the deflections of each segment add up. As opposed to these two models above, the beam model is not sensitive to the number of segments. Consequently, the Young's moduli identified for both 10 and 20 segments are the same and therefore they are presented using a single plot in Fig. 10(c).

Note that, for a given number of segments and optimization goal (e.g., the tip fit), the variation of the identified parameters with the changing force is relatively small in all three models. This slight variation is observed to be mainly due to experimental errors such

as the resolution of the imaging system and the localization of the black stripes on the shaft.

4.2. Performance in modeling needle deflection

During a needle insertion simulation, the forces are not known a priori. Thus, the goal of a needle deformation model is to successfully predict needle deflections for a wide range of possible loads using only a single set of fixed parameters. In this paper, we use a single identified parameter for each model. These parameters, identified in the previous section, vary slightly with the applied force. Consequently, the effect of using a single fixed parameter for all applied loads is studied next. In total, six parameters have been identified for three different models with 10 and 20 segments each.

As seen in Fig. 10, the parameters identified using the tip fit and the area fit are close, thus either of these error measures could be used to determine a fixed parameter for each model. The mean of the parameter values identified using the tip fit method was chosen as the fixed parameter in simulating each model for evaluation.

Each fixed parameter was then used to simulate the needle deflection for all the seven different tip loads and these simulated deflections were compared with the experimental results. Fig. 11 shows these simulated deflections for the three models with 20 segments along with the experimentally observed needle configurations. The tip and area errors for 10 and 20 segments using fixed parameters are presented in Fig. 12.
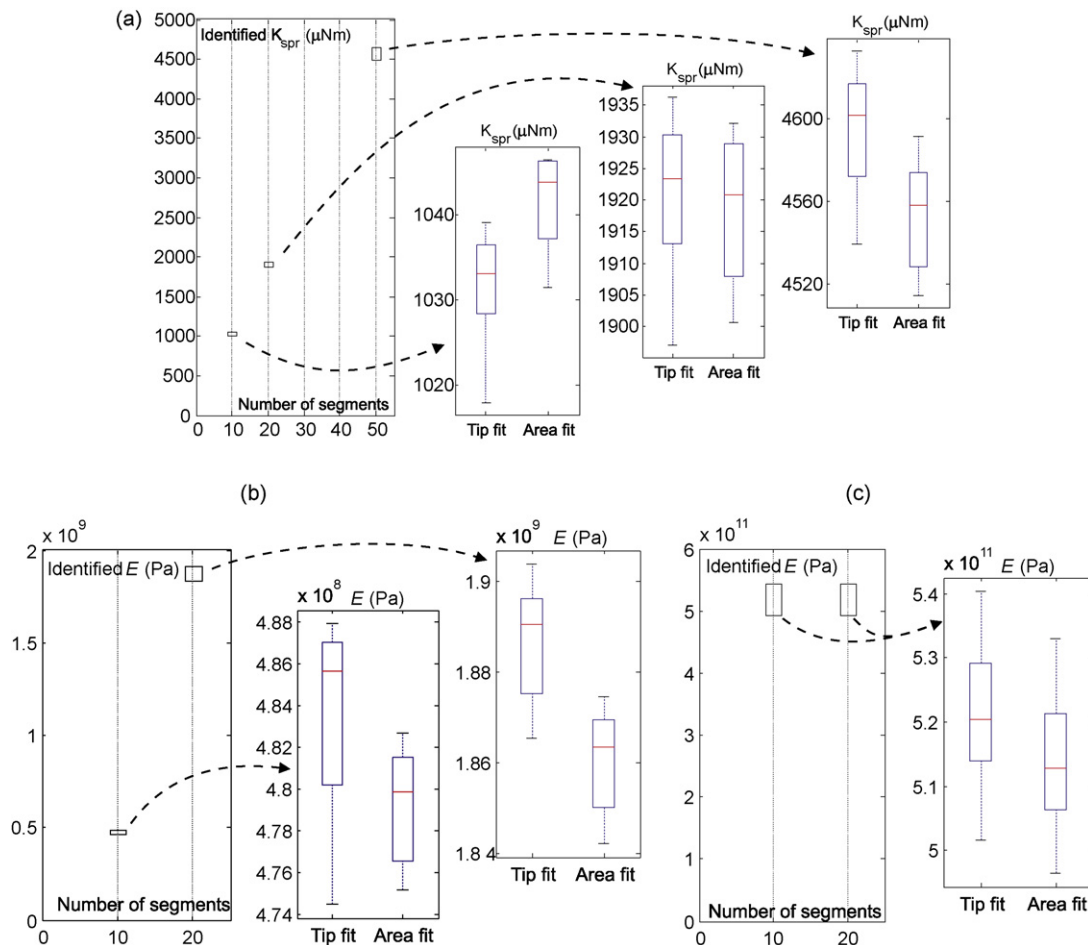

Fig. 10. Distribution of identified Young's moduli and spring constants by minimizing tip and area errors for each bending experiment using a different load. Boxes extend from the lower quartile to the upper quartile value with the median marked. Whiskers show the full extent of data for models (a) 10/20/50 segment spring, (b) 10/20 segment triangular, and (c) 10/20 segment beam (having equal values). The extents of values are also shown in separate figures for each model to facilitate comparing them within full range of values.
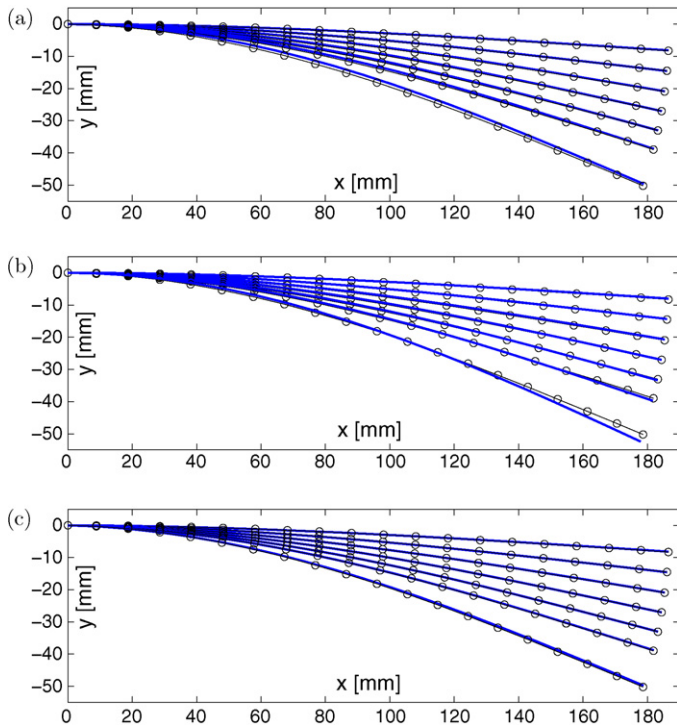
Fig. 11. The experimental deformed needle posture (circles) and the simulated needle (thicker solid lines) using the mean value of identified parameters. (a) The triangular element model with a 21×2 mesh. (b) The nonlinear beam model with 20 elements. (c) The angular springs model with 20 segments.

5. Discussion

Thanks to the fast computation of the presented models, and in particular, the angular springs model, they can easily be integrated into real-time medical training simulation systems. Due to their high accuracy, they can also be used in simulations for needle steering and path planning.

Computationally, the beam element model is more efficient than the triangular/tetrahedral element model. Note that a beam
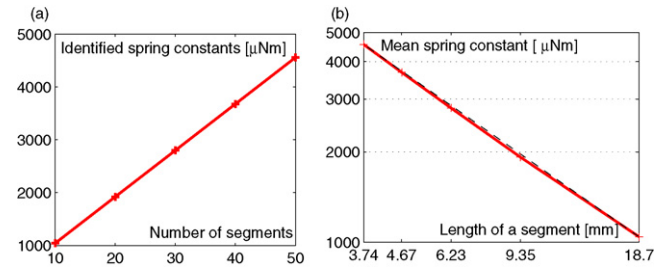

Fig. 13. (a) Mean angular spring constants identified using 10, 20, 30, 40, and 50 segments and (b) a log–log plot of mean spring constants as a function of segment length (dashed-line is a line fitted to the first and the last values).

element and a triangular element both have 6×6 stiffness matrices in 2D and, similarly in 3D, a tetrahedral element and a 3D beam element both have 12×12 stiffness matrices. However, modeling a needle using triangles/tetrahedra requires more elements than the beam element approach. For instance, if the needle is modeled in 2D using a mesh of $2n$ nodes (resulting in $n - 1$ segments), the tangent stiffness matrix will be $4n \times 4n$. In contrast, an equivalent beam model with $n - 1$ elements will result in a $3n \times 3n$ stiffness matrix.

Extension to 3D escalates this computational discrepancy, since a significantly larger number of elements are required for tetrahedral FEM to model the same number of segments in 3D, whereas the beam model and, similarly, the angular springs model use the same number of nodes and elements both in 2D and 3D. Furthermore, achieving an accurate and symmetric 3D model requires many tetrahedral elements [4], whereas the beam and angular springs models are inherently symmetric. Also note that, assuming the needle twist to be negligible facilitates the beam element and the angular springs models since the dimensions of the beam element stiffness matrix can be reduced as shown in Appendix A and, in the angular springs case, skipping the computations involving the twist angle accelerates the convergence of the system in (33) by decreasing the number of unknowns. However, the tetrahedral model does not benefit from this simplification.

In our simulations, the beam element and the angular springs models often converged in fewer iterations than the triangular element model. Not only is the angular springs model robust requiring at most 6 iterations in our simulations, but its each iteration
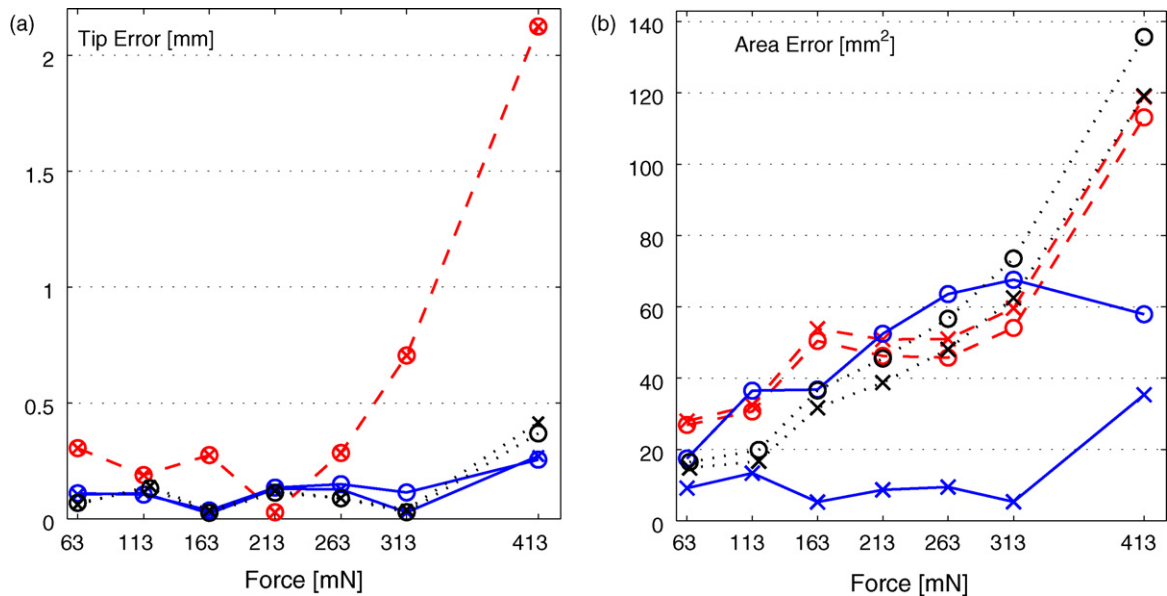

Fig. 12. The tip (a) and area (b) error comparison of the three models (dotted-lines for the triangular FEM, dashed-lines for the beam FEM, and solid-lines for the spring model) simulated using the mean value of identified parameters with 10 and 20 segments (marked with circles and crosses, respectively).

is also computed very fast since it consists of forward vector-algebraic equations with few trigonometric functions, that can be implemented using look-up tables, if necessary. Indeed, during a coupled tissue–needle simulation, the forces on the needle change smoothly. Therefore, an initial needle-posture guess from the previous time instant is often close to its final solution and thus generally only a single iteration is required to find the new equilibrium state.

There are alternative methods to Picard's method that was used to solve (34) for the angular springs model. In particular, a physically based method based on potential energy could be developed using (25) as a starting model. The equilibrium configuration of the system would satisfy (33), with guaranteed convergence.

The identified Young's modulus did not change with the number of elements in the beam element model. Therefore, the beam element model can be used in an adaptive deformation simulation scheme. In this scheme, the simulation starts with a minimum number of elements and, as the needle perforates the tissue and interacts with more tissue, the number of elements is increased (as done in [7]).

Note that the given angular springs model can be simplified to neglect the twist along the shaft by ignoring/zeroing the angles α_i. This is a valid assumption for many needles since the twist is often negligible due to the high shear modulus of the needle shaft and/or small twisting torques acting on it.

The angular springs model as presented deals with force loads only. Nevertheless, torque loads can easily be integrated in the formulation by extending the Jacobian definition in (31) as follows:

$$\underline{\tau} = \mathbf{J}' \begin{bmatrix} \underline{f} \\ \underline{g} \end{bmatrix} \tag{36}$$

where $\mathbf{J}$ is now a $6 \times 3n$ Jacobian matrix and $\underline{g}$ is the vector of torque loads at joints.

Although in our formulation of the angular springs model the force loads were considered only at nodes/joints, in practice, forces at any location on the model can be accommodated, since their corresponding moment arms can be calculated regardless of them being applied at a joint or not.

In our experiments, a single tip force was applied on the needle. However, soft tissue applies a distribution of force along the needle shaft during a needle insertion. In order to employ the presented discrete models, these forces need to be integrated on the discrete needle node locations first. Such integration is common in the FEM literature. Then, these multiple discretized forces can be applied on the discrete needle model. Both FEM models and angular springs are known to perform stably with multiple loads applied [20,23]. Overall, the coupled needle–tissue system is solved in an iterative scheme, which therefore takes the insertion history into account. Such a coupled system was presented in [4].

The experiments were conducted with the needle stylet within the needle cannula. The needle is expected to bend more without the stylet (as also observed in our preliminary observations). Experiments can be repeated in order to identify the (expectedly lower) model parameters for the same needle without the stylet. Subsequently, for a bending simulation where the stylet is partially inside the cannula, the corresponding parameter can be used for the sections of the needle with and without the stylet.

In this paper, equal length segments were used in the angular springs model that led to equal spring constants for all the joints. It should be noted that both bending and twisting spring constants of a segment are defined for a specific segment length and they are both inversely proportional to this length as formulated in Appendices B and C. This relation between segment length and the bending spring constant was further studied (Section 5.1) to devise a spring-constant approximation scheme for any given length. It was confirmed that the bending spring constant is inversely proportional to the segment length.

5.1. Approximating the angular spring constants

It is not always possible to determine the best segment length to use in a needle simulation at the time the bending model is developed. For a specific simulation, a finer or coarser model than the one for which parameters were initially identified may be required. For each segment length, running simulations to identify individual parameters may not be feasible. Furthermore, segment lengths may need to be adjusted online during a simulation. Therefore, identifying a relation between the segment length and the spring parameter is beneficial. For this, the angular springs model, being the most accurate in modeling needle bending and the fastest to simulate, is studied next.

The angular spring constants identified using 10, 20, 30, 40, and 50 segments are plotted in Fig. 13(a). In this figure, only the mean value of constants identified through different loading experiments are shown since the other values lie within 1% range as also observed in Fig. 10(c–e) for the case of 10, 20, and 50, respectively. It is seen that the mean identified spring constant has a linear relation with the number of segments, which is inversely proportional to the segment length. This relation between the spring constant and the segment length is indeed expected from (49).

The change of this mean spring constant with segment length is presented in Fig. 13(b) in a log–log scale. Recall that the effective bending needle shaft is 186.7 mm. As seen in this figure, the angular spring parameter for a given segment length can be interpolated easily from the known values. For instance, if the parameters for 20, 30, or 40 segments are identified using a line fit (dashed line in Fig. 13(b)) to the values of 10 and 50 segments, the interpolated values fall within 2.5% of the spring parameters that were actually identified through individual simulations.

6. Conclusions

Three different models were presented to simulate the deformations of a needle. The first two models use tetrahedral and beam elements, while the third model uses rigid bars connected through angular springs. All the models can preserve the needle length during moderately large deformations. The efficacy of the models in simulations of needle bending was evaluated through experiments during which several lateral forces were applied to a brachytherapy needle and the resulting deformations were recorded. The model parameters – Young's modulus for the FEM-based models and spring constants for the angular springs model – were identified to fit each model to these experimental data. The lateral tip error and the area error were independently minimized to find the parameters defining each model. Later, one single parameter value was extracted for each model and the needle deformations simulated using these values were compared to the experimental deformations. A scheme for intrapolating spring constants from values identified through simulations is also presented.

The angular springs model demonstrated the highest accuracy compared to the other two models. Furthermore, this method is computationally the most efficient and it is the simplest to implement. It was shown that the Young's modulus in the tetrahedral/triangular model is significantly dependent on the number of elements. However, the same parameter is independent of the segment length in the beam element. This property can be used in adaptive simulation to increase the speed.

The models are capable of simulating the needle twist. However, twist is often negligible in medical procedures and it is not validated through our experimental setup.

Acknowledgement

Appendix A. Euler-bernoulli beam element

The strain energy in a beam can be written as:

$$U = \frac{1}{2} \int_V \left[E\epsilon_{xx}^2 + 4G\left(\epsilon_{xy}^2 + \epsilon_{xz}^2\right) \right] dV, \tag{37}$$

where E and G are the Young's and shear moduli, respectively. Substituting (9)–(11) in (37), one can write the strain energy as [25]:

$$U = \frac{GJ}{2}\int\left(\frac{\partial\alpha_0}{\partial x}\right)^2 dx + \frac{EA}{2}\int\left(\frac{\partial u_0}{\partial x}\right)^2 dx$$
$$+\frac{EI_z}{2}\int\left(\frac{\partial^2 v_0}{\partial x^2}\right)^2 dx + \frac{EI_y}{2}\int\left(\frac{\partial^2 w_0}{\partial x^2}\right)^2 dx$$
$$+\frac{EA}{2}\int\left[\left(\frac{\partial u_0}{\partial x}\right)\left(\frac{\partial v_0}{\partial x}\right)^2 + \left(\frac{\partial u_0}{\partial x}\right)\left(\frac{\partial w_0}{\partial x}\right)^2\right]dx \tag{38}$$
$$+\frac{EA}{8}\int\left[\left(\frac{\partial v_0}{\partial x}\right)^4 + \left(\frac{\partial w_0}{\partial x}\right)^4 + 2\left(\frac{\partial v_0}{\partial x}\right)^2\left(\frac{\partial w_0}{\partial x}\right)^2\right]dx$$

where A is the cross-sectional area, and $J = I_y + I_z$ where I_y and I_z are the second moments of inertia about the y and z axes, respectively. By substituting (12)–(15) in (38), the beam strain energy can be written as a function of nodal variables. Using the virtual work principle, the relation between the nodal variables and nodal forces/torques can be derived by symbolically differentiating the strain energy with respect to the nodal variables. Based on the structure of the equations for a beam element (interpolation functions and energy equation), this can be written in the form of (16) which is detailed as follows:

$$\underline{f} = \begin{bmatrix} \mathbf{K}^{11}_{(2\times2)} & \mathbf{K}^{12}_{(2\times2)} & \mathbf{K}^{13}_{(2\times4)} & \mathbf{K}^{14}_{(2\times4)} \\ \mathbf{K}^{21}_{(2\times2)} & \mathbf{K}^{22}_{(2\times2)} & \mathbf{K}^{23}_{(2\times4)} & \mathbf{K}^{24}_{(2\times4)} \\ \mathbf{K}^{31}_{(4\times2)} & \mathbf{K}^{32}_{(4\times2)} & \mathbf{K}^{33}_{(4\times4)} & \mathbf{K}^{34}_{(4\times4)} \\ \mathbf{K}^{41}_{(4\times2)} & \mathbf{K}^{42}_{(4\times2)} & \mathbf{K}^{43}_{(4\times4)} & \mathbf{K}^{44}_{(4\times4)} \end{bmatrix}\underline{u} \tag{39}$$

$$\underline{u} = [u_p\, u_{p+1}\, \alpha_p\, \alpha_{p+1}\, v_p\, \phi_p\, v_{p+1}\, \phi_{p+1}\, w_p\, \psi_p\, w_{p+1}\, \psi_{p+1}]' \tag{40}$$

$$\underline{f} = [f_p^x f_{p+1}^x\, \tau_p^x \tau_{p+1}^x f_p^y\, \tau_p^y f_{p+1}^y\, \tau_{p+1}^y f_p^z\, \tau_p^z f_{p+1}^z\, \tau_{p+1}^z]' \tag{41}$$

where $\underline{u}$ is the vector of nodal variables; f^x, f^y, and f^z are the nodal forces; and τ^x, τ^y and τ^z are the nodal torques. The blocks of the stiffness matrix $\mathbf{K}$ can be calculated as follows [24]:

$$\mathbf{K}^{11}(i,j) = EA\int_L \dot{N}_i\, \dot{N}_j\, dx, \tag{42}$$

$$\mathbf{K}^{22}(i,j) = GJ\int_L \dot{N}_i\, \dot{N}_j\, dx, \quad \mathbf{K}^{2t} = \mathbf{K}^{t2} = \mathbf{0}\forall_{t\neq2}, \tag{43}$$

$$\mathbf{K}^{31}(i,j) = 2\,\mathbf{K}^{13}(i,j) = EA\int_L \dot{v}_0\, \dot{N}_i\, \dot{M}_j\, dx, \tag{44}$$

$$\mathbf{K}^{33}(i,j) = EI_z\int_L \ddot{M}_i\, \ddot{M}_j\, dx + \frac{1}{2}EA\int_L \dot{v}_0^2\, \dot{M}_i\, \dot{M}_j\, dx, \tag{45}$$

$$\mathbf{K}^{34}(i,j) = \mathbf{K}^{43}(j,i) = \frac{1}{2}EA\int_L \dot{v}_0\, \dot{w}_0\, \dot{M}_i\, \dot{M}_j\, dx, \tag{46}$$

where L is the element length; $(\dot{\ }) = \partial/\partial x$ and $(\ddot{\ }) = \partial^2/\partial x^2$. Blocks $\mathbf{K}_{14}$, $\mathbf{K}_{41}$, and $\mathbf{K}_{44}$ are computed similarly to (44) and (45) by substituting w_0 for v_0 and I_y for I_z.

During the bending of a cantilever beam, such as the needle, no stretching occurs on the beam's neutral axis. Therefore, the strain component ϵ_{xx} in (9) should be equal to zero on the beam axis. However, this constraint cannot be met since v_0 and w_0 are interpolated by cubic functions while a linear interpolation function is employed for u_0. As a result, *membrane locking* occurs resulting in an over-stiff element [24]. One solution for the membrane locking problem is to use one-point Gauss quadrature or reduced integration for the calculation of the sub-matrices of $\mathbf{K}$ that include $\dot{v}_0$ or $\dot{w}_0$ in (44)-(46)[24]. Other parts can still be integrated using two-point Gauss quadrature.

As seen in (43), nodal twists and axial torques (the second row/column blocks of the $\mathbf{K}$ matrix) form a separate linear set of equations that is independent of the other variables, i.e. the lateral forces and torques. Therefore, if the twist angles or the twisting torques are negligible, these rows/columns responsible for twist can be removed to decrease the dimension of the stiffness matrix.

Appendix B. Angle of deflection for a bending moment

Consider a short section of a beam bent under a constant uniform bending moment τ_b. Fig. 14 shows its neutral axis of length L, that is located along a radius of curvature ρ. Let c be the distance of the neutral axis from the outer fibre. From the similarity of the arcs, we obtain the following:

$$\frac{L+\delta}{L} = \frac{\rho+c}{\rho} \quad \Rightarrow \quad \frac{\delta}{L} = \frac{c}{\rho} \tag{47}$$

The fibre strain $\epsilon(x)$ of a fibre at a radial distance x to the neutral fibre is given as:

$$\epsilon(x) = \frac{\tau_b x}{EI} \tag{48}$$

where E is the Young's modulus of the material and I is the moment of inertia of the section. Substituting (47) in the definition of the outer fibre strain $\epsilon(c) = \delta/L$, which is the amount of elongation divided by the initial length, gives $\epsilon(c) = c/\rho$. Substituting this in (48) for a fibre distance of c results in:

$$\epsilon(c) = \frac{\tau_b c}{EI} = \frac{c}{\rho} \quad \Rightarrow \quad \frac{\tau_b}{EI} = \frac{1}{\rho}. \tag{49}$$

An arc of angle ω at radius ρ has a length $L = \omega\rho$. Thus, (49) can be rewritten as follows:

$$\frac{\tau_b}{EI} = \frac{\omega}{L} \quad \Rightarrow \quad \omega = \frac{\tau_b L}{EI}. \tag{50}$$

Note that the bending angle ω is equal to the angle of curvature θ. Thus, the linear relation between the bending moment and the angle of deflection can be written as $\theta = \tau_b/k_b$ where $k_b = EI/L$.
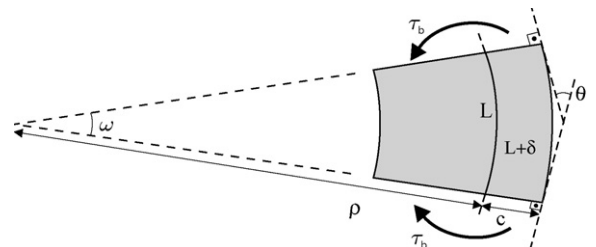

Fig. 14. A short section of a bent cantilever.

Appendix C. Angle of deflection for a torsional (twisting) moment

The angular deflection α of a shaft under torsional moment M can be expressed as:

$$\alpha = \frac{584 L \tau_t}{G D^4} = \frac{\tau_t}{k_\alpha} \tag{51}$$

where L is the length of the twisting section, G is the shear modulus of the material, and D is the shaft radius.

Conflict of interest statement

The authors declare that they have no competing interests.

References

[1] Alterovitz R, Pouliot J, Taschereau R, Hsu IC, Goldberg K. Needle insertion and radioactive seed implantation in human tissue: simulation and sensitivity analysis. In: IEEE Int conf on robotics and automation, vol. 2. 2003. p. 1793–9.
[2] DiMaio SP, Salcudean SE. Needle insertion modeling and simulation. IEEE Trans Robotics Autom: Special Issue Med Robotics 2003;19: 864–75.
[3] Webster RJI, Kim JS, Cowan NJ, Chirikjian GS, Okamura AM. Nonholonomic modeling of needle steering. Int J Robotics Res 2006;25:509–25.
[4] Goksel O, Salcudean SE, DiMaio SP. 3D simulation of needle–tissue interaction with application to prostate brachytherapy. Comput Aided Surg 2006;11(6):279–88.
[5] Dehghan E, Wen X, Zahiri-Azar R, Marchal M, Salcudean SE. Needle insertion interaction modeling using ultrasound-based motion estimation: Phantom study. Comput Aided Surg 2008;13(5):265–80.
[6] Dehghan E, Salcudean SE. Needle insertion parameter optimization for brachytherapy. IEEE Trans Robotics 2009;25(2):303–15.
[7] Glozman D, Shoham M. Image-guided robotic flexible needle steering. IEEE Trans Robotics 2007;23:459–66.
[8] Okamura A, Simone C, O'Leary M. Force modeling for needle insertion into soft tissue. IEEE Trans Biomed Eng 2004;51:1707–16.
[9] Crouch JR, Schneider CM, Wainer J, Okamura AM. A velocity-dependent model for needle insertion in soft tissue. In: Medical image computing and computer assisted intervention. 2005. p. 624–32.
[10] Dehghan E, Goksel O, Salcudean SE. A comparison of needle bending models. In: Medical image computing and computer assisted intervention. 2006. p. 305–12.
[11] Alterovitz R, Branicky M, Goldberg K. Motion planning under uncertainity for image-guided medical needle steering. Int J Robotics Res 2008;27(11–12):1361–74.
[12] Alterovitz R, Lim A, Goldberg K, Chirikjian GS, Okamura AM. Steering flexible needles under Markov motion uncertainty. In: Int Conf on intelligent robots and systems. 2005. p. 120–5.
[13] Park W, Kim JS, Zhou Y, Cowan NJ, Okamura AM, Chirikjian GS. Diffusion-based motion planning for a nonholonomic flexible needle model. In: IEEE Int Conf on robotics and automation. 2005. p. 4600–5.
[14] DiMaio SP. Modelling, simulation and planning of needle motion in soft tissues. Ph.D. thesis, Univ. of British Columbia; 2003.
[15] Yan KG, Podder T, Xiao D, Yu Y, Liu T-I, Cheng C. An improved needle steering model with online parameter estimator. Int J Comput Assisted Radiol Surg 2006;1:205–12.
[16] Abolhassani N, Patel RV, Farzam A. Minimization of needle deflection in robot-assisted percutaneous therapy. Med Robotics Comput Assisted Surg 2007;3(2):140–8.
[17] Kataoka H, Washio T, Audette M, Mizuhara K. A model for relation between needle deflection, force, and thickness on needle penetration. In: Medical image computing and computer assisted intervention. 2001. p. 966–74.
[18] Slocum AH. Precision machine design. SME 1992.
[19] Huang X, Yu TX, Lu G, Lippmann H. Large deflection of elastoplastic beams with prescribed moving and rotating ends. Proc Instn Mech Eng C: J Mech Eng Sci 2003;217(9):1001–13.
[20] Anjyo K, Usami Y, Kurihara T. Simple method for extracting the natural beauty of hair. ACM Comput Graphics 1992;26(2):111–20.
[21] Anshelevich E, Owens S, Lamiraux F, Kavraki LE. Deformable volumes in path planning applications. In: IEEE Int Conf on robotics and automation. 2000. p. 2290–5.
[22] Bro-Nielsen M, Cotin S. Real-time volumetric deformable models for surgery simulation using finite elements and condensation. Comput Graphics Forum (Proc of Eurographics'96) 1996;15(3):57–66.
[23] Zienkiewicz OC, Taylor RL. The finite element method: solid mechanics, vol. 2. 5th ed. Butterworht-Heinemann; 2000.
[24] Reddy JN. An introduction to nonlinear finite element analysis. Oxford University Press; 2004.
[25] Sharf I. Geometrically non-linear beam element for dynamics simulation of multibody systems. Int J Numer Methods Eng 1996;39:763–86.
[26] Sciavicco L, Siciliano B. Modeling and control of robot manipulators. 2nd ed. Springer; 2000.
[27] Lagarias J, Reeds JA, Wright MH, Wright PE. Convergence properties of the Nelder-Mead simplex method in low dimensions. SIAM J Optim 1998;9(1):112–47.